Estimates of spatial variation in evaporation using satellite-derived surface temperature and a water balance model

Laurens M. Bouwer,[1]* Trent W. Biggs[2][†] and Jeroen C. J. H. Aerts[1]

[1] *Institute for Environmental Studies, Faculty of Earth and Life Sciences, Vrije Universiteit, Amsterdam, The Netherlands*
[2] *International Water Management Institute, c/o ICRISAT, Patancheru, Andhra Pradesh, India*

Abstract:

Evaporation dominates the water balance in arid and semi-arid areas. The estimation of evaporation by land-cover type is important for proper management of scarce water resources. Here, we present a method to assess spatial and temporal patterns of actual evaporation by relating water balance evaporation estimates to satellite-derived radiometric surface temperature. The method is applied to a heterogeneous landscape in the Krishna River basin in south India using 10-day composites of NOAA advanced very high-resolution radiometer satellite imagery. The surface temperature predicts the difference between reference evaporation and modelled actual evaporation well in the four catchments ($r^2 = 0.85$ to $r^2 = 0.88$). Spatial and temporal variations in evaporation are linked to vegetation type and irrigation. During the monsoon season (June–September), evaporation occurs quite uniformly over the case-study area ($1.7-2.1$ mm day^{-1}), since precipitation is in excess of soil moisture holding capacity, but it is higher in irrigated areas ($2.2-2.7$ mm day^{-1}). In the post-monsoon season (December–March) evaporation is highest in irrigated areas (2.4 mm day^{-1}). A seemingly reasonable estimate of temporal and spatial patterns of evaporation can be made without the use of more complex and data-intensive methods; the method also constrains satellite estimates of evaporation by the annual water balance, thereby assuring accuracy at the seasonal and annual time-scales. Copyright © 2007 John Wiley & Sons, Ltd.

INTRODUCTION

Evaporation dominates the water balance and governs the availability of water resources in arid and semi-arid areas (Budyko, 1974; Sala *et al*., 1992; Milly, 1994; Reynolds *et al*., 2000). Consequently, small changes in actual evaporation can lead to large changes in surface water flows. Spatial and temporal variations in evaporation may be related to changes in land cover (Gordon *et al*., 2003), land use (Vörösmarty and Sahagian, 2000), and climate (Milly and Dunne, 2001). Therefore, efficient management of water resources depends on accurate estimation of evaporation and its changes with land use, water management, and climate. As water demand for both irrigation and domestic use is increasing, evaporation simulations are urgently needed. Furthermore, requirements for irrigation in water-scarce regions can be better assessed if spatial information on evaporation is available for an entire catchment.

Actual evaporation can be estimated from remote-sensing data using surface energy balance models (e.g. Bastiaanssen *et al*., 1998; Su, 2002, McCabe *et al*.,

2005). However, most of these methods require many parameters and variables as input, including wind speed and aerodynamic resistance. Over large areas, data for such parameters are often not available or are difficult to collect. And although physically based in theory, some of these approaches require calibration to 'wet' and 'dry' patches of land, where evaporation is assumed to be maximum and zero respectively. For instance, the SEBAL method (Bastiaanssen *et al*., 1998) has been applied most successfully for large, homogeneous irrigated areas in arid and semi-arid climates, where the assumptions about evaporation from the wet and dry pixels are likely to be accurate. Identification of pixels with zero evaporation may not be possible in areas or seasons with high rainfall. Conversely, identification of a pixel where all incoming radiation is converted to evaporation (a 'wet pixel') may be difficult to impossible in heterogeneous landscapes during dry periods. Deviations from the wet and dry pixel assumptions may cause over- or under-estimation of evaporation.

Quantification of errors in and validation of satellite-based evaporation estimates is difficult due to the frequent lack of actual evaporation measurements by Bowen ratio or eddy correlation towers. Alternatively, satellite-based evaporation estimates can be compared with annual or monthly water balances based on observed precipitation and runoff. Use of simple hydrological models, such as

* Correspondence to: Laurens M. Bouwer, Institute for Environmental Studies, Faculty of Earth and Life Sciences, Vrije Universiteit, De Boelelaan 1087, 1081 HV, Amsterdam, The Netherlands.
E-mail: laurens.bouwer@ivm.falw.vu.nl
† Present address: INTERA Incorporated, Niwot, Colorado, USA.

SWAT and BASINS, has become increasingly common in management situations, and fusion of these techniques with spatially distributed evaporation estimates from satellite imagery would be of interest in numerous management situations. However, the resources and expertise required to implement more complex surface-energy balance algorithms often restricts their use to a few images over a given study area, which precludes the development of seasonal and annual evaporation estimates that can be compared with observations of the annual water budget based on precipitation and runoff. It is these seasonal and annual evaporation estimates by cover type that are the most important for applied water management. Simplified methods to estimate evaporation from satellite imagery, constrained by simple water balance modelling, would allow more frequent application of satellite methods over seasonal and annual time-scales.

Simplified approaches to estimate spatial variation in evaporation may yield results comparable to more complex, physically based methods, and allow for validation by water balance observations and models. Some studies have related surface properties such as temperature and the normalized difference vegetation index (NDVI) to evaporation. For instance, Szilagyi *et al.* (1998) showed that variation in evaporation is related to changes in NDVI. Loukas *et al.* (2005) used a water balance model to relate estimated monthly actual evaporation to variation in NDVI for selected small watersheds. Di Bella *et al.* (2000) calculated monthly actual evaporation from a water balance and made spatial estimates from a linear regression with NDVI and surface temperatures. But the predictive power of the regressions from the above-mentioned studies is often limited because the vigour of the vegetation as registered by NDVI is only partly related to actual evaporation, in particular over shorter time spans. These studies also did not account for effects of variation in incoming radiation energy that may affect evaporation rates. Therefore, we propose to relate the difference between actual evaporation and reference evaporation to surface temperature, as this approximates more closely the energy balance models but requires a relatively limited amount of input data.

The goal of this paper is to present a method that makes an empirical catchment-scale estimate of the spatial distribution of evaporation. The objective is to estimate seasonal and annual evaporation using satellite imagery, constrained by water balance calculations. The method simplifies satellite-based evaporation estimates over large areas and over seasonal to annual time-scales. This method may prove useful for applied management situations where model estimates of evaporation are available, but where expertise and resources are not available to implement more labour-intensive algorithms to estimate evaporation from satellite imagery. We apply the method to four catchments in a heterogeneous irrigated landscape in southern India. The method uses a relationship between surface temperature and evaporation analogous to more complex surface energy balance algorithms. A water balance model is used to calibrate a

regression model at the catchments scale, relating evaporation to surface temperatures based on remote sensing. By combining the catchment-scale water balance estimate of evaporation with the spatial information provided by remote-sensing data, an estimate can be made of small-scale spatial variation in evaporation. This variation is then attributed to different vegetation types. The remote-sensing data do not provide an independent measure of actual evaporation, but rather a quantitative understanding of how actual evaporation is spatially distributed and how it is related to a variety of land-cover types.

METHODS

The following steps were taken in developing spatial evaporation estimates:

- Actual evaporation is first estimated from a daily water balance model based on using observed precipitation data. The water balance is calibrated to observed runoff from gauging stations.
- These actual evaporation values are then averaged over the catchment and compared with a time-series of catchment-average radiometric surface temperatures derived from optical remote-sensing images (NOAA advanced very high-resolution radiometer (AVHRR)). A linear regression equation relates these surface temperatures to the average actual evaporation from the water balance model.
- Using the surface temperature images, estimates of the spatial distribution of actual evaporation are constructed using the regression equations for predicting evaporation values for each individual pixel.
- Next, the timing and magnitude of evaporation is estimated for different land-cover types that have been identified in the study area using high-resolution satellite imagery and ground-truth data.

Daily water balance model

We use the STREAM model (Aerts *et al.*, 1999) for estimating actual evaporation. This model calculates the water balance for the soil water, groundwater, and surface water according to the formulas provided by Thornthwaite and Mather (1957). Variants of the Thornthwaite–Mather approach have been used in modelling river basins with scarce data, including the Singkarak–Ombilin River basin in Indonesia (Perangi-nangin *et al.*, 2004) and Volta basin in Africa (Taylor *et al.*, 2006), as well as other river basins. The STREAM model has been successfully applied in other river basins (e.g. Aerts *et al.*, 2006; Winsemius *et al.*, 2006). The model was previously set up to investigate long-term variation in the water balance of the entire Krishna River basin (Bouwer *et al.*, 2006). For the current study the model was developed at a resolution of 1 km^2. The main model input is formed by two layers of raster data, consisting of the spatial distribution of daily precipitation

based on observations and flow direction based on a digital elevation model (DEM). Unlike the original STREAM model (Bouwer *et al.*, 2006), our implementation of the model did not use crop coefficients for each cell; rather, our objective was to determine catchment-average evaporation and use the average evaporation to calibrate thermal satellite imagery to calculate actual evaporation. See also the discussion of the calibration of the model in the 'Water balance modelling' section.

The water balance model calculates the upper limit of actual evaporation from reference evaporation. The reference evaporation for each of the four study catchments is adjusted by using a reduction factor. The reduction factor is a single factor for each catchment, and limits the maximum actual evaporation by adjusting the reference evaporation. The original STREAM model uses a crop coefficient that varies for each cell in the model according to vegetation type, rather than a single reduction factor. Since we want to keep all methods as straightforward as possible, reference evaporation ET_0 is calculated from observed air temperature and extraterrestrial radiation only, using the formula developed by Hargreaves and Samani (1985):

$$ET_0 = 0.0023 \times 0.408 R_a (\bar{t} + 17.8)(t_{max} - t_{min})^{0.5} \quad (1)$$

where R_a (MJ m^{-2} day^{-1}) is extraterrestrial radiation, $\bar{t}$ (°C) is the mean daily temperature, t_{min} (°C) is the daily minimum temperature and t_{max} (°C) is the daily maximum temperature. This equation neglects the effect of albedo on ET_0.

The constants 0.0023 and 17.8 were found empirically, and the constant 0.408 converts the radiation to evaporation equivalents in millimetres (Droogers and Allen, 2002). Daily extraterrestrial radiation can be estimated using the equations in Allen *et al.* (1998).

Actual evaporation is calculated as either the reference evaporation ET_0 if the amount of precipitation is greater than reference evaporation, or as the change in the soil water balance if precipitation is less than ET_0. Changes in soil moisture storage depend on precipitation surplus or deficit. Excess precipitation is separated between direct runoff, or quick flow, and delayed runoff, or base flow. Base flow is routed to the stream at a pace according to a recession coefficient, which determines base flow as a function of groundwater storage. The model does not keep track of storage of water in reservoirs; such storage would be calibrated as either soil moisture storage or groundwater storage. The small reservoirs in the study area are generally used to recharge groundwater or are temporary storages that empty every year. As such, they may be thought of and represented as a soil moisture store that is depleted more gradually over the year, or as a groundwater store that contributes to runoff at a rate determined by the recession coefficient. Therefore, this storage can be adjusted by the recession coefficient and the reduction coefficient. Since annual surface runoff is generally low (4–26% of precipitation), evaporation will be dominated by changes in soil moisture storage, and

the effect of including reservoir storage as soil moisture would have a minimal impact on predicted evaporation estimates.

Remote-sensing estimates of surface temperature

The surface temperature of the Earth can be calculated from remote-sensing data. The temperature of the surface as observed by satellites differs from actual surface temperatures due to the absorption and emission of thermal infrared radiance by the atmosphere. A split window technique can be used to adjust for this deviation and uses the difference in atmospheric attenuation between the 10.30–11.30 and the 11.50–12.50 μm spectrums. Various formulations for the split window technique have been developed and tested (Pozo Vázquez *et al.*, 1997). Since the goal of this study is not the most accurate determination of surface temperature, but rather the spatial and temporal variations in temperature in the case-study areas, we use the equation developed by Price (1984), which has been assessed to have an accuracy of 2–3 K:

$$T_b = T_4 + 3.33(T_4 - T_5) - 273.15 \quad (2)$$

where T_b (°C) is the brightness temperature, T_4 (K) is the brightness temperature in AVHRR channel 4 and T_5 (K) is the brightness temperature in channel 5.

Since the Earth does not behave like a perfect blackbody, the radiation energy of the surface has to be corrected for emissivity differences of the surface. Radiometric surface temperature T_0, therefore, is calculated from brightness temperature using

$$T_0 = \frac{T_b}{\varepsilon_0^{0.25}} \quad (3)$$

where T_0 is the radiometric surface temperature and ε_0 is the surface emissivity. The surface emissivity ε_0 can be calculated from NDVI using the empirical equation from Van de Griend and Owe (1993):

$$\varepsilon_0 = 1.0094 + 0.047 \ln(NDVI) \quad (4)$$

Actual evaporation and surface temperatures

By considering an energy balance, radiometric surface temperature can be related to actual evaporation. The surface energy balance can be written as (e.g. Jackson *et al.*, 1977; Seguin and Itier, 1983)

$$R_n = G + H + ET_a \quad (5)$$

where R_n (W m^{-2}) is the net radiation, G is the soil heat flux, H is the sensible heat flux and ET_a is actual evaporation.

A linear relationship exists between the sensible heat flux and the difference between surface temperature and air temperature:

$$H = \rho_{air} c_p \frac{\Delta T_{air}}{r_{ah}} \quad (6)$$

where ρ_{air} is the moist air density, c_p is the specific heat at constant pressure, ΔT_{air} is the difference in

air temperature between the evaporating surface and a reference height above the evaporating surface (usually 2 m), and r_{ah} is the aerodynamic resistance.

Bastiaanssen *et al*. (2002) proposed that ΔT_{air} can be estimated using the radiometric surface temperature T_0 from

$$\Delta T_{air} = \alpha + \beta T_0 \quad (7)$$

Since the spatial variation in aerodynamic resistance r_{ah} is unknown, and ρ_{air} and c_p are constant for a given temperature, we combine them into a simplified, two-parameter linear equation:

$$H = a + bT_0 \quad (8)$$

Substitution into Equation (5) gives

$$R_n - ET_a = a + bT_0 \quad (9)$$

where ET_a is the catchment-average actual evaporation as estimated by the STREAM model. The soil heat flux is ignored, but on a daily basis it can be considered to be zero.

The main challenge in application of thermal remote-sensing imagery to estimate evaporation is the determination of α and β (Bastiaanssen *et al*., 2002), or a and b in our case, which vary with every image and vegetation surface type. The SEBAL approach, for instance, uses wet and dry pixels to solve Equation (6), where the sensible heat flux is assumed to be equal to zero or R_n respectively. Here, we use instead the catchment-average ET_a from the STREAM model and the reference evaporation in place of net radiation:

$$ET_0 - ET_a = a + bT_0 \quad (10)$$

We test for the ability of reference evaporation and surface temperature (Equation (10)) to estimate catchment-average actual evaporation as calculated by the STREAM water balance model. We use a time-series of catchment-average T_0 from satellite imagery and ET_a from the STREAM model to determine a and b, and then apply the catchment-average a and b to the entire satellite image to calculate spatially distributed evaporation.

One major assumption of our simplified model is that a and b are constant for different vegetation types. This may not be the case if α, β or the aerodynamic resistance r_{ah} differ for different vegetation types. r_{ah} varies with vegetation height and wind speed. However, spatial variations in r_{ah} are difficult to estimate accurately over a regional scale, particularly for heterogeneous pixels, where definition of average vegetation height and friction velocities is not possible or perhaps meaningful from the standpoint of a physically based model of sensible heat transport. Although more complex formulations of r_{ah} are possible that include atmospheric instability via the Monin−Obukhov equations (see Bastiaanssen *et al*. (2002)), r_{ah}, α and β are treated as calibration parameters in the SEBAL approach. Here, we combine the calibrated parameters into two simplified parameters

(a and b), and determine the value of those parameters with Equation (10).

CASE-STUDY AREA AND DATA

The Krishna River basin

The Krishna River basin extends over $258\,948$ km^2 in southern India and terminates at a delta in the east in the Bay of Bengal (Figure 1). The climate in the basin is subtropical with plentiful rainfall, accumulating to 3000 mm in the mountains of the Western Ghats, and arid conditions in the basin interior. Runoff of the Krishna River basin over the past century has been highly variable, and total annual runoff at the basin end has decreased dramatically in recent decades, which can be attributed to increasing water consumption for irrigation. It has been estimated that water consumption for irrigation has caused a persistent decrease in annual runoff of up to 61% (Bouwer *et al*., 2006).

Four subcatchments in the Krishna River basin were selected for this study: the Musi, Halia, Jewangi and Madhira, which are located just north of the downstream reaches of the Krishna River (Figure 1). The catchments range in size from 1850 km^2 (Madhira) to $11\,501$ km^2 (Musi).

The three cropping seasons in the region consist of the Kharif during the monsoon (June−November), Rabi during post-monsoon (December−March), and a short summer season from April to May. Irrigated agriculture is dominated by rice, but includes some supplemental irrigation of cotton, chilli, orchards, and irrigated dry crops like sorghum, oilseeds, and corn. Average annual precipitation over the period 1992−1999 varied from 700 mm in the Musi catchment, to 637 mm in the Halia catchment and to 784 mm in the Jewangi catchment, whereas the Madhira catchment received considerably more precipitation, i.e. 1014 mm on average per year (Table I). Groundwater irrigation and small reservoirs dominate the irrigated areas in the Jewangi, Halia, and Musi catchments (Biggs *et al*., 2006).

The command area of the Nagarjuna Sagar irrigation project overlaps with the Madhira and Musi catchments, and the observed discharge downstream of the overlap includes return flows from irrigation (Figure 1). The Madhira catchment is located at the tail end of the
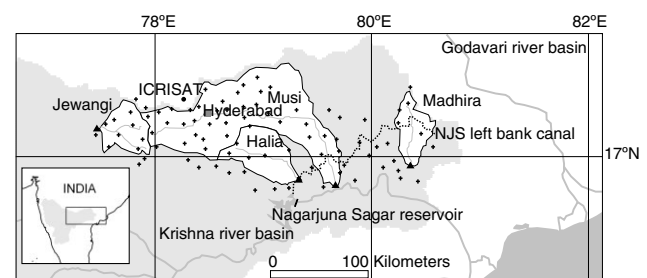

Figure 1. Study area location, with the four catchments and the locations of precipitation stations (crosses). The Nagarjuna Sagar (NJS) left-bank canal is indicated by the dotted line

Table I. Discharge gauging stations in the four catchments. Catchment surface areas according to the Indian Central Water Commission

River	Discharge station	Latitude (°N)	Longitude (°E)	Discharge data	Area (km^2)	Average precipitation (mm)
Musi	Dameracherla	16·74	79·67	1988–2000	11 501	700
Halia	Halia	16·79	79·33	1988–1996	3 100	637
Jewangi	Kagna	17·26	77·47	1988–1996	1 920	784
Madhira	Wyra	16·92	80·36	1988–2000	1 850	1014

Nagarjuna Sagar left-bank canal, where flows are low, whereas the Musi occurs at the head end of the project and shows evidence of significant return flow. The Musi catchment also has inflow of about 10 Mm^3 per month from the Krishna River basin via water supply to the city of Hyderabad, which creates a wastewater-irrigated area of approximately 200 km^2 (Van Rooijen *et al.*, 2005). Hyderabad is one of the fastest growing cities in India, with a population currently at 6·8 million. Consequently, there are also plans to import water to the city from the adjacent Godavari River basin (Figure 1).

Data

A DEM from the Shuttle Radar Topography Mission (Van Zyl, 2001) was used to determine the flow direction in each grid cell of the STREAM water balance model. The DEM was resampled from the original 90 m × 90 m resolution to 1 km × 1 km resolution.

The maximum soil water-holding capacity was taken from a soil map compiled by the USDA (available at http://soils.usda.gov/use/worldsoils/mapindex/whc.html) as 200 mm m^{-1} for the entire study area. This estimate also reflects the effect of the many small barrages and storages for water in the area. There may be spatial differences in soil type, but the effect on differences in evaporation between locations is later solved by using remote sensing; the main goal is the estimation of catchment-average evaporation and water-holding capacity, which does not require a representation of spatial variations in soil type. The effects due to soil or vegetation type on differences in evaporation between catchments are solved by other calibration parameters, such as the reduction coefficient.

The records of 90 rainfall stations cover most of the area of the four catchments (Figure 1) and they contain no gaps in their daily records over the period 1992–2001. The precipitation data were interpolated to a resolution of 1 km^2 using inverse distance-weighted averaging. Rainfall stations are located in the headquarters of administrative units called Mandals; the centre of each Mandal was taken as the location of observation. No use was made of the DEM for the interpolation of precipitation data, since there are data available for a reasonable number of rainfall stations (approximately one station per 200 km^2) and the relief differences between the stations are modest (maximum 10–20 m).

Daily data for maximum and minimum temperatures, as well as pan evaporation, for the period 1992–2001 were taken from the climate station at the compound of the International Crops Research Institute for the Semi-Arid Tropics (ICRISAT) in Patancheru, northeast of Hyderabad (17·53 °N, 78·27 °E, altitude 545 m; see Figure 1). A time-series of the average 10-day precipitation over the Musi catchment is shown in Figure 2, together with the reference evaporation as calculated from the ICRISAT temperature data, using Equation (1).

Daily discharge data for the four catchments were obtained from yearbooks of the Central Water Commission (CWC; see Table I).

The United States Geological Survey provides 10-day composites of NOAA AVHRR imagery (available at http://edcsns17.cr.usgs.gov/1KM/comp10d.html), consisting of daily afternoon images with a 1·1 km^2 resolution at nadir. Data for all five AVHRR channels are provided, as well as computed NDVI. The 10-day composites were assembled for three periods: 1 April 1992–30 September 1993, 1 February 1995–31 January
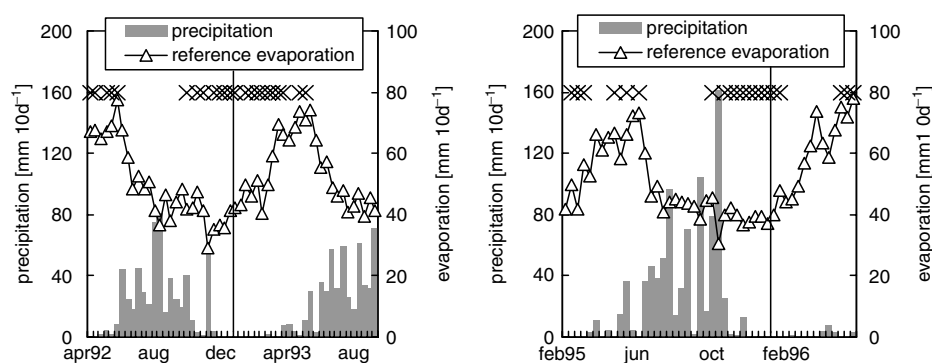

Figure 2. Total precipitation over the Musi catchment and reference evaporation per 10 days for 1992–1993 and 1995–1996. Crosses indicate the AVHRR composite dates that were used

1996, and 1–31 May 1996. The composites were created using maximum-NDVI compositing, thereby reducing the number of cloud-contaminated pixels (Holben, 1986). These data have already undergone radiometric calibration and atmospheric correction; for details, see Eidenshink and Faundeen (1994). Owing to clouds, in particular in the period June–September, and owing to missing data, many composites had to be discarded from the analysis, resulting in gaps in the time-series. A total of 43 composites were suitable out of the 93 composite images that were available (see the crosses in Figure 2). Using nearest-neighbour resampling and a linear mapping function, data were resampled to a resolution of 1 km^2.

Polygons of different land-cover types were visually delineated for the case-study area using the Landsat TM mosaic data from the GeoCover-LC 1990 dataset (see http://www.mdafederal.com/geocover/geocoverlc/) and ground-truth information from field visits over the period 2003–2005. These polygons were used to calculate actual evaporation for different land-cover types based on the estimates of evaporation using the surface temperature images.

RESULTS

The data described in the previous section were used to set up the hydrological model STREAM, to assess surface temperatures, and to identify land-cover types for the four catchments. This section first describes the calibration of the STREAM model and the results of the water balance modelling over the period 1992–2000. Second, regressions between evaporation and surface temperatures are presented for two periods, i.e. 1992–1993 and 1995–1996. Finally, estimates of temporal and spatial variations in evaporation are made on the basis of these regressions, and temporal patterns are developed from these estimates for different land-cover types.

Water balance modelling

Three parameters were adjusted for each catchment to calibrate the water balance model to the observed runoff: a reduction coefficient, a separation coefficient and a recession coefficient. The reference evaporation (Equation (1)) is multiplied by a different reduction coefficient for each catchment to obtain an adjusted reference evaporation that reflects differences in total annual actual evaporation between the catchments depending on vegetation characteristics. The separation coefficient is the fraction of daily effective precipitation that becomes direct runoff, which includes both overland and subsurface storm flows with short response times. The remaining runoff becomes base flow. The recession coefficient determines the response time of the base flow. The values of the calibration parameters for the individual catchments are listed in Table II.

The objectives of the calibration were first to match the simulated total annual runoff with the observed runoff using the reduction coefficient. The second objective is to match the seasonal patterns of low and high flows by adjusting the separation and recession coefficients. Simulated daily runoff was aggregated to 10-day periods, in order to compare actual evaporation with the surface temperatures as estimated from the remote-sensing data. The performance of the calibrated STREAM model was assessed using the efficiency coefficient of Nash and Sutcliffe (1970).

The calibration results are listed in Table III. Accurate simulations were obtained for runoff from the Madhira and Jewangi catchments (efficiency coefficient $R^2 = 0.72$ and $R^2 = 0.86$ respectively). The simulations for the Musi and Halia catchments were not as good ($R^2 = 0.44$ and $R^2 = 0.50$). In the Musi catchment this is probably due to the fact that return flows from canal irrigation are not incorporated in the model, which leads to an underestimation of runoff in the post-monsoon period.

The recession coefficient is particularly high in the Musi catchment (Table II), which reflects return flow from the Nagarjuna Sagar (NJS) irrigation project in the

Table II. Calibration coefficients for the STREAM water balance model

River	Reduction	Separation	Recession
Musi	0·849	0·3	130
Halia	1·092	0·6	90
Jewangi	1·089	0·7	30
Madhira	0·800	0·3	90

Table III. Calibration results and average annual water balance in the four catchments

Parameter	Musi	Halia	Jewangi	Madhira
Period	1992–1999	1992–1995	1992–1995	1992–1999
n[a]	303	159	159	303
Observed runoff (mm)	75	29	59	267
Simulated runoff (mm)	75	29	59	267
Efficiency R^2	0·44	0·50	0·86	0·72
Precipitation (mm)	700	652	770	1014
Irrigation input (mm)	21	0	0	?
Actual evaporation (mm)	583	601	674	681
Simulated runoff/precipitation	0·11	0·04	0·08	0·26
Evaporation/precipitation	0·83	0·92	0·88	0·67

[a] The number of 10-day streamflow observations that were compared with the simulations.

post-monsoon period. The small share of direct runoff in the Musi and the Madhira catchments, represented by a low separation coefficient, is a reflection of the fact that much water is being stored and used for irrigation. The Musi and the Madhira catchments have some portion of their drainage area in the NJS irrigated command area. For the Musi catchment this is 431 km^2 of the total 11 501 km^2. Inflows come from the main left-bank canal, which originates in the NJS reservoir (see Figure 1) and traverses the lower portions of both catchments. The return flow from this canal increases the base flow at the discharge station, particularly during the post-monsoon Rabi season (December–March). A medium irrigation project with a reservoir capacity of 131 × 10^6 m^3 is located some 50 km upstream of the discharge station in the Musi catchment, and significant retention of runoff occurs in an estimated 1500 small tanks in the catchment (International Water Management Institute (IWMI), unpublished data).

Observed inflow to the Musi medium command area over 1994–1999 was approximately 20 mm on average. The observed canal input from the NJS reservoir was approximately equal to runoff on average between 1994 and 2001. The irrigated command area in the Musi catchment is fully saturated rice cultivation, which likely has a high runoff coefficient compared with rain-fed uplands in the rest of the Musi catchment area.

An estimated two-thirds of the rainfall is evaporated in the Madhira catchment, whereas 83–92% is evaporated in the other three catchments (Table III). The exclusion of return flows in the modelling would not substantially affect the estimates of actual evaporation, since precipitation and evaporation are the dominant components of the water balance. Therefore, errors in the canal inputs or runoff values would result in relatively small errors in evaporation, as the accuracy of the model depends primarily on the accuracy of the precipitation input.

Surface temperatures and actual evaporation

Using Equation (10), regressions were made between the difference between the catchment-average reference evaporation (estimated using Equation (1)) and the estimated actual evaporation (from the water balance model) and the catchment average radiometric surface temperatures as estimated using the remote-sensing images. The regressions were made for the two periods of 1992–1993 and 1995–1996 for the four catchments (Figure 3). The difference between the reference and estimated actual evaporation is linearly and strongly related to catchment average surface temperatures ($r^2 = 0.88$ and $r^2 = 0.85$, $p < 0.0001$). Despite the fact that the STREAM model does not account for the additional inflow from the NJS project and possibly higher evaporation amounts in the Musi and Madhira catchments, regressions for the Musi and Madhira catchments do not differ substantially from regressions for the Halia and Jewangi catchments. This can be shown by comparing the sum of squares produced by two equations for all catchments for the periods 1992–1993 and 1995–1996 with the sum of squares produced by eight equations for each individual catchment for the periods 1992–1993 and 1995–1996. There is no significant improvement by using separate regressions for each catchment, which was tested by an F-test (Ott and Longnecker, 2001), where $F = 1.85$ and $F_{crit} = 2.30$ ($p < 0.01$).

The coefficients a and b (Figure 3) were established using 23 images over 1992–1993 and 20 images over 1995–1996. Separate regressions for the periods 1992–1993 and 1995–1996 reduced the sum of squares by 30% compared with one combined regression, which is statistically significant ($F = 36.04$ and $F_{crit} = 4.75$, $p < 0.01$). This difference between the two periods may be caused by differences in atmospheric conditions, surface conditions, or errors in the estimation of actual evaporation from the water balance model, resulting in different evaporation rates for the same surface temperature. Also, differences in soil moisture between years would influence the actual evaporation. Agriculture and irrigation practices between the two periods may also be different, and affect some of the parameters above, such as soil moisture. This suggests that the calibrations need to be performed for each year for best accuracy.
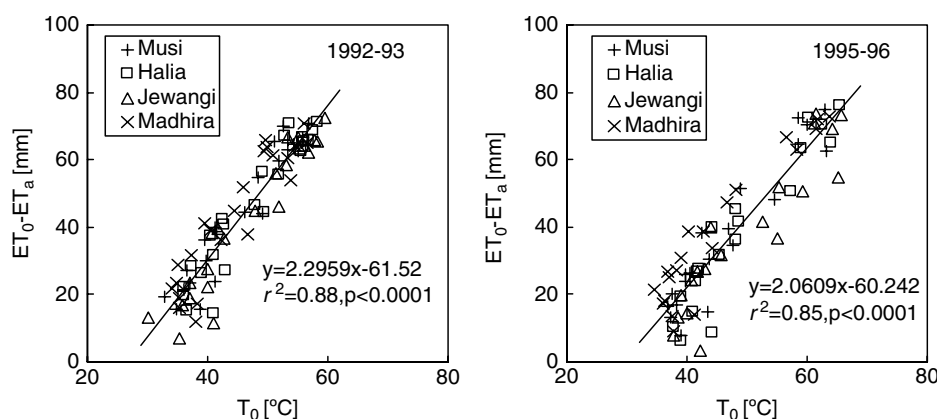

Figure 3. Correlation between modelled difference between reference and actual evaporation and surface temperature, both averaged for the four catchments for 1992–1993 and 1995–1996. Evaporation is in millimetres per 10 days
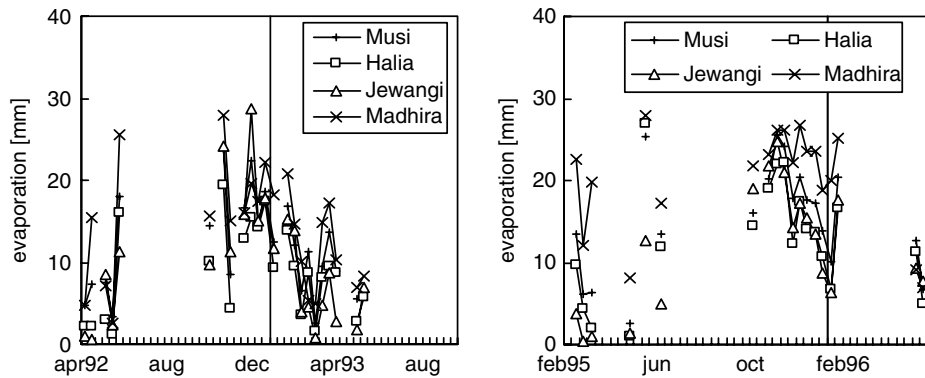
Figure 4. Total estimated evaporation per 10 days for the four river basins

Spatially distributed actual evaporation was calculated for each 10-day composite surface temperature image using Equation (10) for the periods 1992–1993 and 1995–1996. The average evaporation values over time were calculated for each catchment (Figure 4). Estimates of actual evaporation using the surface temperatures could be made for only part of the year, since much of the data had to be omitted, mostly due to clouds. Particularly little information is available for the early part of the Kharif season (June–August).

The regression equations based on 10-day average values have a standard error of the estimate of 6·8 mm (15% for the average value of $ET_0 - ET_a$, or ± 0.68 mm day^{-1}) and 8·4 mm (22%, ± 0.84 mm day^{-1}) for the periods 1992–1993 and 1995–1996 respectively. The actual uncertainty of the estimates is larger, as there are more sources of uncertainty that affect the estimates (see the paragraphs on error sources in the 'Discussion' section).

Estimates of spatial variation in evaporation

The maps of actual evaporation generated from the surface temperature images can be used to assess the spatial characteristics of evaporation over time. Evaporation rates were estimated for the monsoon, post-monsoon and dry seasons as the average of evaporation values of the available images for the corresponding dates. Average evaporation during the monsoon (Kharif) season in 1992 (June–November) was almost uniform over the case-study area (mean evaporation 1·67 mm day^{-1}, standard deviation ± 0.72 mm day^{-1}), but is higher in the irrigated areas (Figure 5, top). In the Rabi season in 1992 (December–March; mean evaporation 1·52 $\pm$ 0·75 mm day^{-1}), most evaporation occurs in the downstream sections, mainly in the NJS command area (Figure 5, middle). During the dry summer season (April–May), less water is evaporated (Figure 5, bottom; mean 1·14 $\pm$ 1·00 mm day^{-1}). The substantial drop in the dry summer season is due to both dry soil conditions and reduced irrigated areas. Many farmers allow their fields to go fallow during the summer season, resulting in lower evaporation rates in irrigated command areas. For Kharif and Rabi in 1995, similar patterns can be observed (Figure 6), except that the average amount of evaporation is higher for the entire images during 1995–1996, caused by a higher average rainfall over the four catchments during 1995–1996 (972 mm) compared with 1992–1993 (709 mm; see also Figure 2). Large water areas, such as open ocean and large reservoirs, are omitted in Figures 5 and 6.

Evaporation for different land-cover types

Different land-cover types in the catchments were identified using the GeoCover dataset (Figure 7) and ground-truth information from field visits over the period 2003–2005. The average evaporation rates per season as estimated from the remote-sensing imagery for representative land-cover types are shown in Table IV and Figure 8. Table V lists the corresponding average NDVI values and radiometric surface temperatures for each land-cover category. We distinguish water and four classes of irrigated land: canal-irrigated crops that obtain water from the NJS reservoir, wastewater-irrigated crops in the Musi catchment, rain-fed agriculture with supplemental groundwater irrigation in the Musi catchment, and mixed rain-fed and irrigated patches of crops in the Halia catchment. Finally, we recognize two types of natural vegetation: rangelands that may overlap with rain-fed crops and the forest area in the Madhira catchment.

Evaporation rates for all land-cover types are highest during the monsoon Kharif season, and decline towards Rabi and the dry season. The highest evaporation rates are observed from open water (4·1–7·0 mm day^{-1}). The values for open water given in Table IV are derived from small patches of water in Figures 5 and 6.

For vegetated surfaces, particularly high evaporation rates can be seen from the forest in the Madhira catchment (up to 3·5 mm day^{-1}), irrigated areas in the Godavari Delta (4·0–4·3 mm day^{-1}), and the canal-irrigated areas that use water from the NJS reservoir (up to 2·9 mm day^{-1}) and wastewater irrigation (up to 3·6 mm day^{-1}). On an annual basis, the canal-irrigated areas in the Musi catchment have nearly the same evaporation amount (796–828 mm) as the wastewater-irrigated areas (735–867 mm), but the rates in wastewater-irrigated areas remain more constant throughout the year (Figure 8). The slightly lower rates in some of the wastewater-irrigated areas may be due to either a high frequency of fallows in the rotation system used in the

Kharif 1992: μ=1.67 mm d^{-1},σ=0.72 mm d^{-1} · Evaporation [mm]

Rabi 1992: μ=1.52 mm d^{-1},σ=0.75 mm d^{-1}

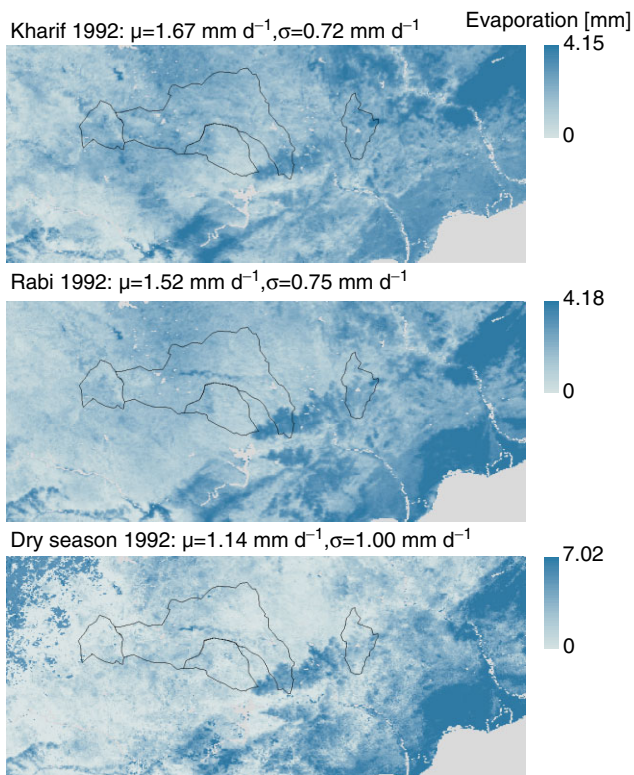Dry season 1992: μ=1.14 mm d^{-1},σ=1.00 mm d^{-1}

Figure 5. Evaporation during Kharif, Rabi and dry season in 1992. Large water bodies are indicated by grey areas. Location of the image is the same as in Figure 1

Kharif 1995: μ=2.12 mm d^{-1},σ=0.87 mm d^{-1} · Evaporation [mm]

Rabi 1995: μ=1.90 mm d^{-1},σ=0.91mm d^{-1}

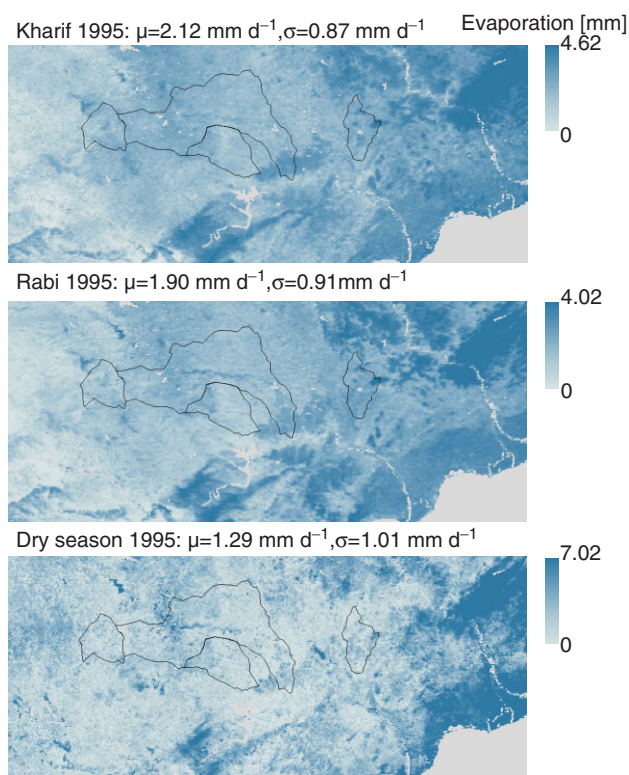Dry season 1995: μ=1.29 mm d^{-1},σ=1.01 mm d^{-1}

Figure 6. Evaporation during Kharif, Rabi and dry season in 1995. Large water bodies are indicated by grey areas. Location of the image is the same as in Figure 1

wastewater-irrigated areas, or to lower transpiration rates caused partly by high-salinity irrigation water.

Overall, evaporation for all land-cover types was higher in 1995–1996 than in 1992–1993, as about 29% more precipitation was available during the monsoon of 1995. The irrigated areas that retrieve their water from the NJS reservoir appear to have a strong decline in evaporation in the dry season of 1995, compared with 1992 (Figure 6, bottom). This could be the result of an underestimation of evaporation for the dry season, as the estimates for the dry season of 1995 are based on the images for May only, which is the driest month.

DISCUSSION

Evaporation rates from irrigated areas as estimated using the satellite imagery are lower than expected from a healthy crop growing in large fields with adequate water supply. Crop coefficients for irrigated rice from the FAO-56 method (Allen *et al.*, 1998) are 1·0 for flooded and initial growth stages, 1·15 during maximum growth, and 0·45–0·75 during senescence and harvest, for a seasonal average of 1·05, or 656 mm (4·4 mm day^{-1}) for a 150-day season. By contrast, our method gives seasonal-average Kharif (monsoon) evaporation rates
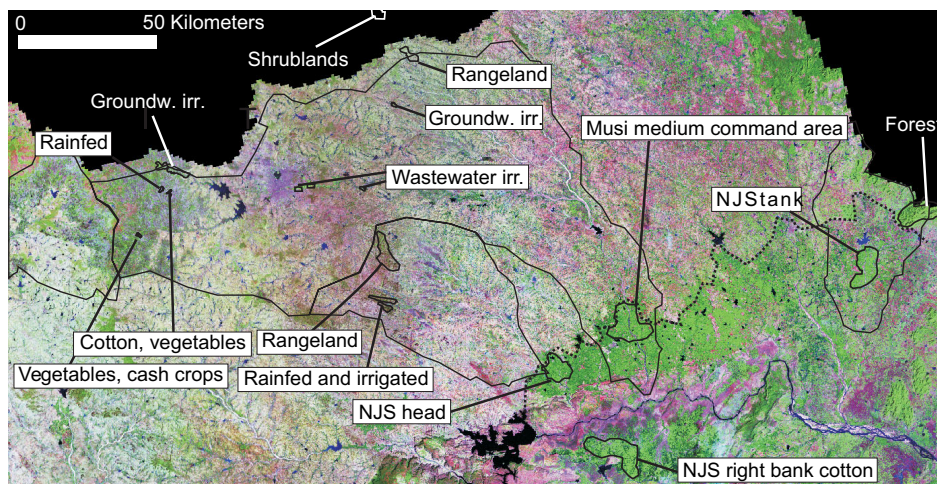

Figure 7. Land-cover types in the study area based on GeoCover 1990 data

Table IV. Evaporation rates (mm day^{-1}) and totals for different land-cover types per season for 1992–1993 and 1995–1996. Category averages are listed with bold headings

	1992–1993				1995–1996			
	Kharif	Rabi	Dry	Total (mm)	Kharif	Rabi	Dry	Total (mm)
Number of images used/of total	4/18	11/12	3/6		6/18	6/12	3/6	
Mean rainfall range over four river basins (mm)	488–742	0–24	43–137	532–903	760–1078	0–1	15–26	804–1239
Reference evaporation	4·5	4·7	7·0	1800	4·5	4·8	6·9	1794
Pan evaporation × 0·7	3·8	4·4	8·2	1695	3·9	4·4	7·4	1669
Open water	4·2	4·1	7·0	1662	4·4	4·0	6·9	1677
Godavari irrigation	4·0	3·8	3·5	1386	4·3	4·0	4·0	1494
NJS canal irrigation	2·2	2·4	1·9	796	2·7	2·4	1·0	828
Halia, rice	2·5	2·6	2·5	914	2·7	2·3	1·2	840
Musi, rice	2·5	2·7	2·1	899	2·8	2·2	1·2	841
Madhira, rice	2·1	1·8	1·3	660	2·6	2·4	1·2	834
Krishna r.b. cotton	1·8	2·4	1·6	709	2·4	2·8	0·5	799
Wastewater irrigation	1·9	2·3	1·8	735	2·4	2·6	2·3	867
Musi, rice	2·0	2·4	2·0	770	2·3	2·7	1·5	827
Musi, rice	1·8	1·9	1·2	627	1·8	2·1	1·2	653
Musi, paragrass	1·7	2·5	2·0	727	2·5	2·6	2·7	922
Musi, paragrass	2·1	2·5	2·2	815	2·8	2·9	3·6	1065
Mixed rain-fed/supplemental irrigation	1·9	1·1	0·4	492	1·9	1·6	0·8	581
Musi, cotton, vegetables	2·2	0·8	0·5	518	1·6	1·4	0·7	509
Musi, vegetables	1·7	1·4	0·1	486	1·9	1·8	0·5	587
Musi, cotton, vegetables	1·6	1·2	0·5	469	2·0	1·8	1·1	643
Musi, cotton, vegetables	2·0	0·9	0·3	495	1·9	1·6	0·8	584
Mixed irrigated and rain fed	2·2	1·7	1·1	665	2·2	2·1	1·2	726
Halia	2·2	1·7	0·9	661	2·2	2·0	1·1	704
Halia	2·1	1·7	1·2	668	2·3	2·2	1·3	748
Rangelands, rain-fed agriculture	1·8	1·5	0·8	551	2·2	1·9	1·0	696
Halia	2·0	1·7	0·9	612	2·3	2·2	1·4	754
Musi, shrubland	2·1	1·9	1·4	692	2·5	2·3	1·6	819
Musi, deer park	1·7	1·7	0·7	548	2·6	2·2	0·8	771
Musi, rangeland	1·6	0·8	0·1	385	1·9	1·6	0·5	572
Musi, rangeland	1·7	1·4	0·7	520	2·0	1·3	0·9	562
Forest Madhira	3·1	2·3	1·7	937	3·5	3·5	1·7	1151

Table V. Average NDVI values and average radiometric surface temperatures for six land-cover categories

	NDVI						Radiometric surface temperature (°C)					
	1992–1993			1995–1996			1992–1993			1995–1996		
	Kharif	Rabi	Dry	Kharif	Rabi	Dry	Kharif	Rabi	Dry	Kharif	Rabi	Dry
Open water	0·03	−0·07	0·00	0·00	−0·07	−0·05	17·8	23·4	15·7	14·5	24·4	32·3
NJS canal irrigation	0·52	0·39	0·24	0·49	0·39	0·21	35·2	37·0	49·1	38·6	36·6	60·9
Wastewater irrigation	0·39	0·35	0·25	0·39	0·37	0·28	36·2	37·9	50·2	39·9	36·3	54·4
Mixed rainfed/supplemental irrigation	0·36	0·25	0·14	0·38	0·34	0·18	36·6	42·5	56·1	42·7	40·6	62·1
Mixed irrigated and rainfed	0·37	0·29	0·15	0·42	0·34	0·19	35·4	39·7	52·7	40·5	38·3	59·8
Rain-fed agriculture and rangelands	0·37	0·24	0·14	0·40	0·33	0·21	36·5	41·0	54·2	40·8	39·0	60·6
Forest	0·56	0·31	0·18	0·55	0·58	0·15	34·8	39·2	51·3	39·6	37·0	61·9

of 4·0 mm day^{-1} and 4·3 mm day^{-1} (crop coefficients of 0·88–0·96) in the Godavari Delta for 1992–1993 and 1995–1996 respectively. Most irrigated areas in the Krishna basin, however, have lower Kharif values, e.g. 2·5 mm day^{-1} in 1992–1993 and 2·7 mm day^{-1} in 1995–1996 (crop coefficient of 0·55–0·61) for irrigated rice at the head end of the Nagurjuna Sagar canal (Table II). In Rabi, evaporation rates from irrigated areas are similar to the Kharif rate of 2·3–2·6 mm day^{-1} (crop coefficients of 0·48–0·56). Our estimates of evaporation

from irrigated rice, however, are only slightly lower than the independent estimates for the early Rabi season by Ahmad *et al.* (2006) over the same study area (2·6–3·3 mm day^{-1}) using the surface energy balance algorithm SEBAL and a Landsat TM image.

The low evaporation and crop coefficients we measured for irrigated areas may be partly due to relatively high humidity over irrigated areas, which can reduce the crop coefficient by up to 10% (Allen *et al.*, 1998). Partial irrigation coverage within each 1 km^2 pixel could also
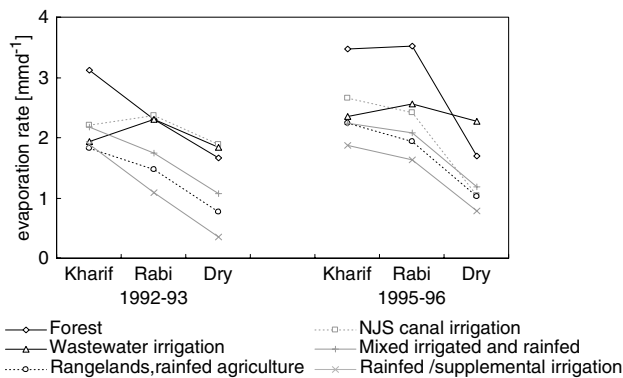
Figure 8. Estimated evaporation rates for some land-cover types per season in 1992 and 1995

explain the low evaporation rates. Even in canal-irrigated areas, only 70–80% of the area is actually irrigated, the rest being a combination of build area, fallows, and other scrub vegetation that likely have lower evaporation rates than the irrigated area (Biggs *et al.*, 2006). Additionally, the irrigated areas in our study had relatively low NDVI values during the monsoon period (0·39–0·52), which suggests either partial irrigation or reduced vegetation vigour in the irrigated command areas. The estimate provided here gives the spatially averaged water consumption over relatively large portions of irrigated areas, which is of interest to water resources planners.

Estimated annual evaporation from open water listed in Table IV (1662–1677 mm year^{-1}) is nearly the same as pan evaporation times a pan coefficient of 0·7 (1669–1695 mm year^{-1}). This suggests that the method is accurate for wet surfaces that have surface temperatures outside the range of calibration; this increases confidence in the evaporation estimates for other surfaces.

Rangelands and rain-fed agriculture show lower evaporation rates during the post-monsoon season (about 29% lower than during the monsoon season), and show a seasonal decline that is similar to the areas with supplemental groundwater irrigation (Figure 8). This suggests that substantial soil moisture storage supplies rain-fed vegetation with water for evaporation well into the Rabi and dry seasons. The purely rain-fed rangeland vegetation in the Musi catchment, however, shows reductions by between 37 and 49% in the post-monsoon Rabi and dry seasons compared with the monsoon Kharif season. This shows that substantial reductions also do occur for natural vegetation due to soil moisture limitation.

The low evaporation in the groundwater-irrigated areas is not necessarily due to low evaporation from irrigated land, but is likely due to a small irrigation fraction in these areas. The pixels in the remote-sensing imagery cover 1 km^2, whereas most groundwater-irrigated plots cover less than 0·01 km^2. Less than 25–40% of groundwater-irrigated classes mapped with coarse-resolution imagery are actually irrigated, the rest being rain-fed uplands (Biggs *et al.*, 2006). Higher resolution imagery would be required to determine the actual evaporation rigorously from small groundwater-irrigated pixels.

Please note that the evaporation rates by land cover are based on limited data. A particularly limited number of images were available for the Kharif season (four images in 1992 and six images in 1995). Since the available images occur during peak vegetation stage (October–January), the estimates for Rabi are likely higher than the true seasonal values that include earlier vegetation growth stages. Compared with the STREAM model output, the estimates using the remote-sensing images are, on average, 37% higher for the Rabi season.

The method used here has two principle sources of error, both related to the values of the parameters *a* and *b* in the regression Equation (10): errors in the STREAM model predictions of evaporation, which could yield errors in the parameters *a* and *b*, and errors produced from the assumption about the spatial and temporal uniformity of *a* and *b*. First, *a* and *b* are calibrated to the STREAM water balance model predictions of actual evaporation for all four entire catchments, so any error on the STREAM evaporation estimates will propagate to produce errors in the satellite-based evaporate estimate. The soil moisture-holding capacity, in particular, governs the rate at which evaporation decreases after the termination of rainfall. Any systematic error in the soil moisture accounting could cause a similar error in evaporation estimation.

Also, the maximum NDVI compositing technique that was used for the surface temperature images does not necessarily give the best estimates of surface temperatures during the 10-day intervals. It does, however, give the temperature associated with the peak in vegetation vigour during those 10 days.

Second, the method assumes that *a* and *b* are constant in space and time, i.e. a constant relationship between radiometric surface temperature and the difference between potential and actual evaporation is assumed (Equation 10). In the SEBAL method (Bastiaanssen *et al.*, 2002), different *a* and *b* parameters are calculated for each image, and the aerodynamic resistance term is allowed to vary over space. However, for our application, spatial heterogeneity in vegetation over 1 km^2 pixels prevents rigorous determination of vegetation height, friction velocities, and aerodynamic resistance. In addition, most vegetation in our study area is cropland, and should have vegetation height in a fairly narrow range (1–2 m). The largest errors will occur where vegetation is substantially different from the average, such as forests. Given the uncertainty in the aerodynamic properties of the vegetation over the study area, we take a parsimonious approach to model formulation. While recognizing that there may be spatial heterogeneity in aerodynamic resistance with different vegetation types (and, therefore, spatial differences for *a* and *b*), we assume that we cannot resolve all spatial heterogeneity with the current data set. Under conditions of parameter uncertainty, we opted for simplification of the model and calibration to the STREAM model estimates. This constrains the seasonal and average evaporation estimation to the observed water balance.

Despite the uncertainty in spatial variations of aerodynamic resistance and *a* and *b*, the evaporation values

from the remote-sensing imagery closely match ground-based measurements for open water (Table IV) and are similar to the expectation for evaporation from vigorous irrigated vegetation in the Godavari Delta. The observation of low evaporation from other irrigated areas, such as the canal-irrigated areas of NJS, requires further validation, but matches energy balance model results in this study area (Ahmad *et al.*, 2006). This suggests that evaporation may be lower than potential evaporation even in well-watered irrigated areas due either to patchiness in the irrigated area within 1 km^2 pixels or to low evaporation from the irrigated vegetation itself. Future investigation could attempt to resolve the issue by measuring biomass accumulation rate of irrigated rice in the command areas and comparing that with satellite-derived estimates of evaporation.

SUMMARY AND CONCLUSIONS

The goals of this research were to present a simplified method for deriving evaporation estimates on a catchment scale by linking a water balance model to surface temperatures based on remote sensing, and to estimate the spatial and temporal variations of actual evaporation for selected catchments in the Krishna River basin. The method emphasizes the use of water balance model-based estimates of evaporation, calibrated to observed precipitation and runoff, to constrain evaporation estimates from satellite imagery over seasonal to annual timescales.

The STREAM water balance model makes reasonable estimates of 10-day total runoff despite the fact that the possible effects of ground-water irrigation, and irrigation return flows from canals crossing catchment boundaries have been ignored.

A series of maps of average surface temperature were constructed from 10-day NOAA AVHRR composites for the period April 1992-May 1993 and February 1995-May 1996. We established relationships between actual evaporation from a water balance model and temporal variation in remotely sensed surface temperatures for 10-day intervals, using the regression equation $ET_0 - ET_a = a + bT_0$, where ET_0 is the reference evaporation, ET_a is the actual evaporation, T_0 is the surface temperature, all estimated for catchment averages, and a and b are coefficients that have single values for all four catchments. These regressions based on 10-day data result in coefficients of determination between $r^2 = 0.85$ and $r^2 = 0.88$ ($p < 0.0001$), which are better than previously reported coefficients for relationships at the catchment scale between monthly evaporation and NDVI (Loukas *et al.*, 2005) or multiple regressions between monthly evaporation and NDVI and surface temperatures (Di Bella *et al.*, 2000). This is probably because our method considers variation in incoming radiation energy and its effects on reference evaporation. Also, we were able to make accurate regressions for a shorter time span of 10-day intervals.

Using these regressions, we created estimates of spatial and temporal variations of 10-day evaporation for the case-study area. During the Kharif season (June–November), evaporation occurs almost equally over the case-study area, but is higher in the irrigated areas. In the Rabi season (December–March) most evaporation occurs in the downstream sections, mainly in the NJS command area, whereas the upstream parts show a substantial reduction in evaporation compared with the monsoon-season values. During the dry summer season, considerably less water is evaporated. The highest evaporation rates are found for forests and for irrigated vegetation within the NJS project areas and for irrigated areas in the adjacent Godavari River basin.

We found evidence of relatively low evaporation rates from irrigated crops compared with the expectation from reference evaporation. Our estimates of actual evaporation from irrigated rice are 39–45% less than predicted by crop coefficients for an unstressed crop. This is most likely because, even in irrigated areas, only 70–80% of the area is actually irrigated, but it could also be due to low evaporation from the irrigated crop itself. Whether rice irrigated with water from NJS really has lower evaporation than healthy rice is an important issue and could be addressed by a more detailed study. For irrigated areas in the adjacent Godavari River basin (see Figure 1), the evaporation rate estimates for the Kharif season more closely resemble crop coefficients of healthy rice. This shows that the method accurately captures maximum evaporation rates from well-watered vegetation. Also, estimated annual evaporation from open water is nearly the same as pan evaporation times a pan coefficient of 0.7, which suggests that our method is accurate for wet surfaces that have surface temperatures outside the range of calibration.

Establishing actual evaporation from rain-fed and irrigated vegetation in more upstream parts of the basin with different climate and irrigation regimes, for instance sugarcane, will help to close the water balance and determine whether evaporation from irrigated surfaces has been underestimated by the method presented here. We also find evidence of lower evaporation from wastewater-irrigated areas compared with other areas irrigated by reservoir water. This may reflect lower transpiration rates in wastewater. Farmer-reported rice yields in the wastewater-irrigated area are 25% less than other irrigated areas, due partly to high salinity. More evidence, such as measurements of total biomass, will be necessary to prove that evaporation is lower from wastewater-irrigated areas, but the current results support the hypothesis that evaporation from wastewater irrigation is lower than from other irrigated areas.

Using this method, a seemingly reasonable estimate of temporal and spatial patterns of evaporation can be made without the use of more complex and data-intensive techniques, though our estimates are calibrated to modelled evaporation, and so are not independent measures of evaporation. The approach formulated in Equation (10) will need to be applied to other areas in order to show

its general applicability. Our method, however, may give more realistic estimates of evaporation than energy balance methods, as it is based on an actual water balance. If a rapid and thorough assessment of water resources needs to be made, it may, therefore, be worthwhile using basic remote-sensing applications in combination with a water balance model.

REFERENCES

Aerts JCJH, Kriek M, Schepel M. 1999. STREAM, spatial tools for river basins and environment and analysis of management options: set up and requirements. *Physics and Chemistry of the Earth, Part B: Hydrology, Oceans and Atmosphere* **24**: 591–595.

Aerts JCJH, Renssen H, Ward PJ, de Moel H, Odada E, Bouwer LM, Goosse H. 2006. Sensitivity of global river discharges under Holocene and future climate conditions. *Geophysical Research Letters* **33**: L19401.

Ahmad MD, Biggs T, Turral H, Scott CA. 2006. Application of SEBAL approach and MODIS time-series to map vegetation water use patterns in the data scarce Krishna River basin of India. *Water Science and Technology* **53**: 83–90.

Allen RG, Pereira LS, Raes D, Smith M. 1998. *Crop evapotranspiration: guidelines for computing crop water requirements*. Irrigation and Drainage Paper No. 56, Food and Agricultural Organisation, Rome.

Bastiaanssen WGM, Menenti M, Feddes RA, Holtslag AAM. 1998. A remote sensing surface energy balance algorithm for land (SEBAL): 1. Formulation. *Journal of Hydrology* **212–213**: 198–212.

Bastiaanssen WGM, Ahmad MUD, Chemin Y. 2002. Satellite surveillance of evaporative depletion across the Indus basin. *Water Resources Research* **38**: 1273.

Biggs TW, Thenkabail PS, Gumma MK, Scott CA, Parthasaradhi GR, Turral HN. 2006. Irrigated area mapping in heterogeneous landscapes with MODIS time series, ground truth and census data, Krishna Basin, India. *International Journal of Remote Sensing* **27**: 4245–4266.

Bouwer LM, Aerts JCJH, Droogers P, Dolman AJ. 2006. Detecting the long-term impacts from climate variability and increasing water consumption on runoff in the Krishna River basin (India). *Hydrology and Earth System Sciences* **10**: 703–713.

Budyko MI. 1974. *Climate and Life*. Academic Press: Orlando.

Di Bella CM, Rebella CM, Paruelo JM. 2000. Evapotranspiration estimates using NOAA AVHRR imagery in the Pampa region of Argentina. *International Journal of Remote Sensing* **21**: 791–797.

Droogers P, Allen RG. 2002. Estimating reference evapotranspiration under inaccurate data conditions. *Irrigation and Drainage Systems* **16**: 33–45.

Eidenshink JC, Faundeen JL. 1994. The 1 km AVHRR global land data set: first stages in implementation. *International Journal of Remote Sensing* **15**: 3443–3462.

Gordon L, Dunlop M, Foran B. 2003. Land cover change and water vapour flows: learning from Australia. *Philosophical Transactions of the Royal Society of London, Series B: Biological Sciences* **358**: 1973–1984.

Hargreaves GH, Samani ZA. 1985. Reference crop evapotranspiration from temperature. *Applied Engineering in Agriculture* **1**: 96–99.

Holben BN. 1986. Characteristics of maximum-value composite images from temporal AVHRR data. *International Journal of Remote Sensing* **7**: 1417–1434.

Jackson RD, Reginato RJ, Idso SB. 1977. Wheat canopy temperature: a practical tool for evaluating water requirements. *Water Resources Research* **13**: 651–656.

Loukas A, Vasiliades L, Domenikiotis C, Dalezios NR. 2005. Basin-wide actual evapotranspiration estimation using NOAA/AVHRR satellite data. *Physics and Chemistry of the Earth* **30**: 69–79.

McCabe MF, Kalma JD, Franks SW. 2005. Spatial and temporal patterns of land surface fluxes from remotely sensed surface temperatures within an uncertainty modelling framework. *Hydrology and Earth System Sciences* **9**: 467–480.

Milly PCD. 1994. Climate, soil water storage, and the average annual water balance. *Water Resources Research* **30**: 2143–2156.

Milly PCD, Dunne KA. 2001. Trends in evaporation and surface cooling in the Mississippi River basin. *Geophysical Research Letters* **28**: 1219–1222.

Nash JE, Sutcliffe JV. 1970. River flow forecasting through conceptual models part I: a discussion of principles. *Journal of Hydrology* **10**: 282–290.

Ott RL, Longnecker M. 2001. *An Introduction to Statistical Methods and Data Analysis*. Duxbury: Pacific Grove.

Peranginangin N, Sakthivadivel R, Scott NR, Kendy E, Steenhuis TS. 2004. Water accounting for conjunctive groundwater/surface water management: case of the Singkarak–Ombilin River basin, Indonesia. *Journal of Hydrology* **292**: 1–22.

Pozo Vázquez D, Olmo Reyes FJ, Alados Arboledas L. 1997. A comparative study of algorithms for estimating land surface temperature from AVHRR data. *Remote Sensing of Environment* **62**: 215–222.

Price JC. 1984. Land surface temperature measurements from the split window channels of the NOAA 7 advanced very high resolution radiometer. *Journal of Geophysical Research* **89**(D5): 7231–7237.

Reynolds JF, Kemp PR, Tenhunen JD. 2000. Effects of long-term rainfall variability on evapotranspiration and soil water distribution in the Chihuahuan Desert: a modeling analysis. *Plant Ecology* **150**: 145–159.

Sala OE, Lauenroth WK, Parton WJ. 1992. Long-term soil water dynamics in the shortgrass steppe. *Ecology* **73**: 1175–1181.

Seguin B, Itier B. 1983. Using midday surface temperature to estimate daily evaporation from satellite thermal IR data. *International Journal of Remote Sensing* **4**: 371–383.

Su Z. 2002. The Surface Energy Balance System (SEBS) for estimation of turbulent heat fluxes. *Hydrology and Earth System Sciences* **6**: 85–99.

Szilagyi J, Rundquist DC, Gosselin DC, Parlange MB. 1998. NDVI relationship to monthly evaporation. *Geophysical Research Letters* **25**: 1753–1756.

Taylor JC, van de Giesen N, Steenhuis TS. 2006. West Africa: Volta discharge data quality assessment and use. *Journal of the American Water Resources Association* **42**: 1113–1126.

Thornthwaite CW, Mather JR. 1957. *Instructions and Tables for Computing Potential Evapotranspiration and the Water Balance*. Publications in Climatology 10. Laboratory of Climatology, Drexel Institute of Technology: Centerton; 183–243.

Van de Griend AA, Owe M. 1993. On the relationship between thermal emissivity and the normalized difference vegetation index for natural surfaces. *International Journal of Remote Sensing* **14**: 1119–1131.

Van Rooijen DJ, Turral H, Biggs TW. 2005. Sponge city: water balance of mega-city water use and wastewater use in Hyderabad, India. *Irrigation and Drainage* **54**: S81–S91.

Van Zyl JJ. 2001. The Shuttle Radar Topography Mission (SRTM): a breakthrough in remote sensing of topography. *Acta Astronautica* **48**: 559–565.

Vörösmarty CJ, Sahagian D. 2000. Anthropogenic disturbance of the terrestrial water cycle. *BioScience* **50**: 753–765.

Winsemius HC, Savenije HHG, Gerrits AMJ, Zapreeva EA, Klees R. 2006. Comparison of two model approaches in the Zambezi River basin with regard to model reliability and identifiability. *Hydrology and Earth System Sciences* **10**: 339–352.